Nano Energy 110 (2023) 108377

Contents lists available at ScienceDirect

Nano Energy

journal homepage: www.elsevier.com/locate/nanoen

Full paper

Crystal structure regulation boosts the conductivity and redox chemistry of T-Nb_2O_5 anode material

Jinghui Chen [a,b], Jiashen Meng [c], Kang Han [a], Fang Liu [d], Weixiao Wang [a], Qinyou An [a,b,*], Liqiang Mai [a,b,*]

[a] State Key Laboratory of Advanced Technology for Materials Synthesis and Processing,Wuhan University of Technology, Wuhan 430070, PR China
[b] Hainan Institute, Wuhan University of Technology, Sanya 572000, PR China
[c] Beijing Key Laboratory of Theory and Technology for Advanced Batteries Materials, School of Materials Science and Engineering, Peking University, Beijing 100871, PR China
[d] NRC, Nanostructure Research Centre, Wuhan University of Technology, Wuhan 430070, PR China

ARTICLE INFO

Keywords:
T-Nb_2O_5
Cobalt doping
Conductivity regulation
Redox chemistry
Fast charging

ABSTRACT

T-Nb_2O_5 as a promising candidate anode has attracted great interest for ultrafast lithium-ion batteries (LIBs) due to its good ion conductivity and safety. However, the relatively inferior electric conductivity and low capacity greatly limit its commercial application. Herein, a trace Co doping strategy is reported to enhance the electric conductivity and redox chemistry of T-Nb_2O_5. The original Nb sites are partially replaced by Co, which endows Co-Nb_2O_5 with high electronic conductivity without affecting the crystalline host structure, meanwhile induces multielectron redoxes of Nb^{5+}/Nb^{4+} and Nb^{4+}/Nb^{3+} during lithium-ion insertion process. As a LIB anode, the resulting Co-Nb_2O_5 nanoparticles display a high discharge capacity (256.1 mAh g^{-1} at 0.1 A g^{-1}), superior rate capability (141.7 mAh g^{-1} at 5 A g^{-1}) and good cycling stability (179.7 mAh g^{-1} at 1 A g^{-1} after 500 cycles). The ultrafast lithium storage and high-capacity electrochemical performance of Co-Nb_2O_5 owing to its high electric conductivity and multielectron redox upon lithiation/delithiation. The selective transition metal doping strategy provides a new direction for the development of new insertion-type oxide anodes towards fast charging and high-capacity LIBs.

1. Introduction

To meet increasing demand for commercialization of Lithium-ion batteries (LIBs), developing advanced batteries with excellent energy density and power density is highly desirable [1,2]. Exploring suitable anode materials with fast kinetics and negligible volume variation is the key to improve rate capability and extend cycling life of LIBs [3]. Insertion-type anode materials are hopeful candidates benefiting from their higher first-cycle coulombic efficiency and longer cycling life [4–9]. As the commercial insertion-type anode materials, graphite electrode are unable to facilitate fast charge under a high rate, due to their relatively low Li^+ diffusion kinetics. Besides, lithium dendrite structures are prone to form on graphite anode at a lower working potential (about 0.1 V vs Li/Li^+), leading to potential security hazards of current utilisted LIBs [10]. Therefore, developing insertion-type anode materials with high safety and fast diffusion kinetics is highly desirable to meet the market needs.

Because of the prominent theoretical capacity (201.7 mAh g^{-1}) and good rate performance, insertion-type niobium pentoxide (Nb_2O_5) is regarded as an appealing anode material for lithium intercalation/deintercalation [11–13]. In previous work, our group compared different polymorphs of Nb_2O_5, including T-Nb_2O_5 (orthorhombic), TT-Nb_2O_5 (pseudohexagonal, PE), and H-Nb_2O_5 (monoclinic, P2/m) and investigated phase effects on lithium storage mechanism of three Nb_2O_5 crystal structures, founding that T-Nb_2O_5 anode delivers higher rate capability and better capacity retention [14]. Dunn and co-workers demonstrated a 40 μm thick T-Nb_2O_5 electrode with great electrochemical performance, which is ascribed to the two-dimensional (2D) lithium-ion migration channel in T-Nb_2O_5 electrode [15]. However, the electrochemical utilization and fast charging capability of T-Nb_2O_5, an electronic insulator, may be restricted for its poor electric conductivity (about 3.4×10^{-6} S cm^{-1} at 27 ℃) [16]. Certainly, great efforts have

* Corresponding authors at: State Key Laboratory of Advanced Technology for Materials Synthesis and Processing,Wuhan University of Technology, Wuhan 430070, PR China.
E-mail addresses: anqinyou86@whut.edu.cn (Q. An), mlq518@whut.edu.cn (L. Mai).

https://doi.org/10.1016/j.nanoen.2023.108377
Received 27 December 2022; Received in revised form 8 March 2023; Accepted 21 March 2023
Available online 23 March 2023

been devoted to enhance electronic conductivity of T-Nb_2O_5 anode materials for LIBs, such as conductive materials coating and solid-solution compounds [17–20]. For example, a 3D Nb_2O_5/holy--graphene composite is demonstrated by a two-step method, in order to enhance electronic conductivity and capacity of pure T-Nb_2O_5 electrode [21]. Although great progress has been made based on electrode structure designs, the practical application of T-Nb_2O_5 in high-energy and fast-charging LIBs is still limited [22–24]. Heteroatomic doping may potentially introduce highly localized reactive sites and improve intrinsic electronic conductivity, to achieve higher electrochemical performance, which has been reported to be an effective strategy for the optimization of Nb_2O_5 anode in other types of batteries [25]. Due to the reduction of Fe and additional space for Li^+ after introducing redox-active dopants into layered oxide CeO_2, the achievable capacity is improved [26]. Such metal doping strategies for T-Nb_2O_5 crystal structure (Ti-Nb-O, V-Nb-O, W-Nb-O, Cr-Nb-O and so on) are accompanied by phase transformations to Wadsley-Roth shear structures, providing different Li^+ transport pathways for lithiation/delithiation [27–31]. Meanwhile, the most studied T-Nb_2O_5 electrodes perform one electron redox per Nb during the electrochemical process, in accord with a theoretical discharge capacity of 202 mAh g^{-1} [32–34]. Metal doping strategy for T-Nb_2O_5 to undergo multi-electron redox in Nb to obtain higher theoretical capacity—as far as we know—has not been investigated in previous work.

In this work, the Co-Nb_2O_5 (T-Nb_2O_5 doped with 2% Co) nanoparticles are synthesized by a mismatched coordination reaction during solvothermal method and thermal decomposition process. Trace Co transition metal dopants occupy the Nb sites with low coordination, which can improve intrinsic electronic conductivity and induce the formation of lower valence state Nb during the lithium intercalation process compared with T-Nb_2O_5, resulting in enhanced fast-charging performance. Co-Nb_2O_5 as a LIB anode material displays higher discharge capacity of 256.1 mAh g^{-1} at 0.1 A g^{-1} and better rate performance (141.7 mAh g^{-1} at 5 A g^{-1}) than those of T-Nb_2O_5 (206.7 mAh g^{-1}, 110.5 mAh g^{-1}). Remarkably, the sample Co-Nb_2O_5 displays high cycling stability after 500 cycles (discharge capacity retention of 90%). *In situ* X-ray diffraction (XRD) testing confirms the introduction of larger ionic radius Co dopants can increase interlayer space and then provide more lithium storage sites during charging/discharging process. *Ex situ* X-ray photoelectron spectroscopy (XPS) spectrum revealed that the high capacity of Co-Nb_2O_5 was attributed to its reaction mechanism of Nb^{5+}/Nb^{4+} and Nb^{4+}/Nb^{3+} multielectron redoxes. Results from density functional theory (DFT) calculations indicated that Co-Nb_2O_5 displays low migration barriers for Li^+ diffusion. This work proposes an effective heteroatomic doping approach to enhance electronic conductivity and boost redox chemistry without changing crystalline host structure, then enhance the fast-charging and high-capacity performance of LIBs.

2. Results and discussion

The overall synthetic route of obtained Co-Nb_2O_5 nanoparticles is illustrated in Fig. 1a. First, during the solvothermal process, amorphous metal-ligand (Co-Nb-BDC) compounds as precursors were synthesized through mismatched coordination reaction between metal ions (Co^{2+}, Nb^{5+}) and organic ligands (1,4-dicarboxybenzene, H_2BDC). Different from crystalline metal-organic framework, the resulting metal-ligand complexes have abundant mismatched bonding angles and metal-based twisted polyhedrals, leading to the formation of amorphous

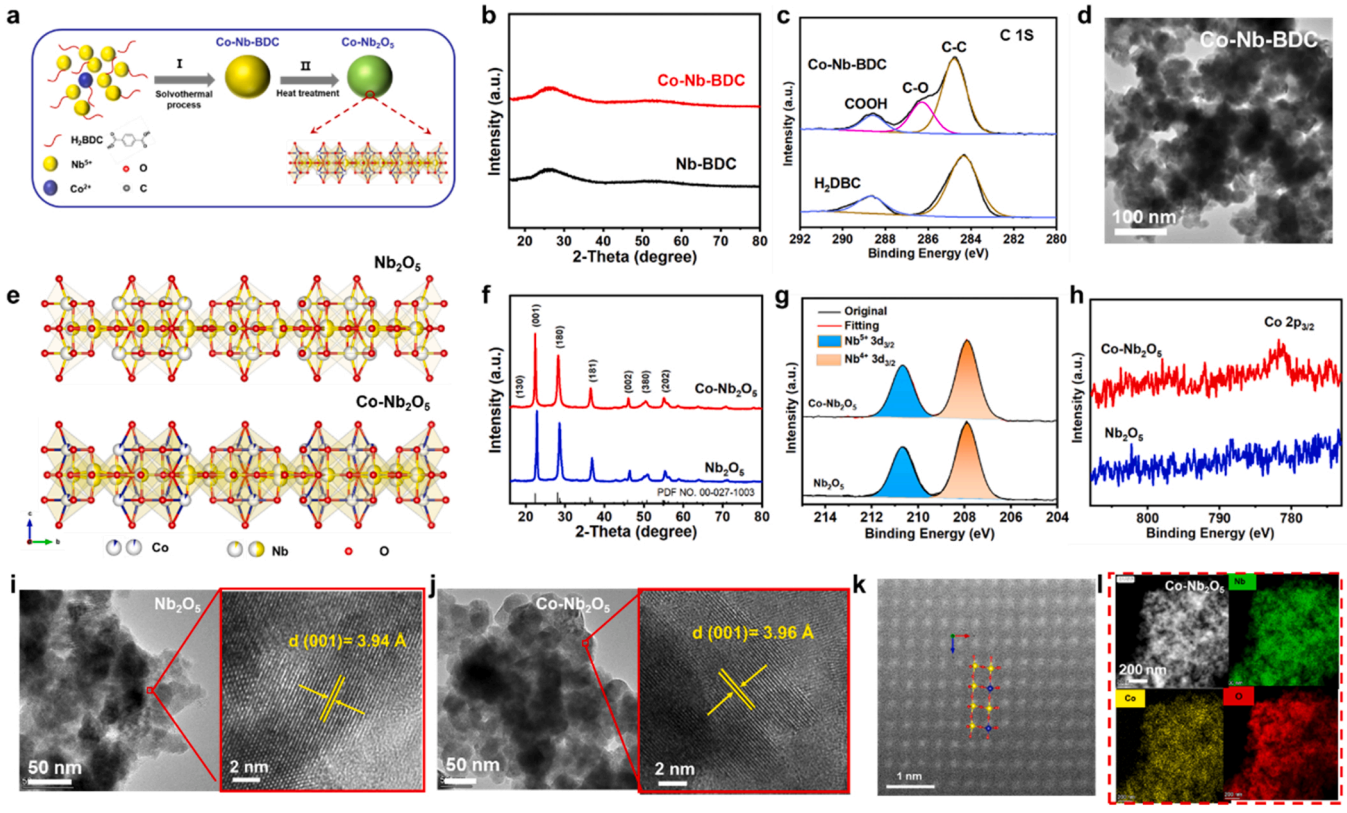

Fig. 1. a) Schematic illustration of synthetic steps of Co-Nb_2O_5. b-d) Characterizations of the Nb-BDC and Co-Nb-BDC complex nanoparticles. b) XRD patterns of Nb-BDC and Co-Nb-BDC. c) High-resolution C 1 s XPS spectra of Co-Nb-BDC complex and H_2BDC, respectively. d) TEM image of Co-Nb-BDC. e-k) Structural characterization of Nb_2O_5 and Co-Nb_2O_5. e) The crystal structure of Nb_2O_5 and Co-Nb_2O_5 with the views along the a-axis. f) X-ray diffraction (XRD) patterns of Nb_2O_5 (in blue) and Co-Nb_2O_5 (in red). g, h) X-ray photoelectron spectroscopy (XPS) analysis of pure Nb_2O_5 and Co-Nb_2O_5. The comparison of g) the Nb 3d spectra and h) the Co 3p spectra for both samples. i) TEM image and HRTEM image of Nb_2O_5 nanoparticles. j) TEM image and HRTEM image of Co-Nb_2O_5 nanoparticles. k) HAADF-STEM image of Co-Nb_2O_5. l) EDS mappings for Nb, Co, and O elements.

materials [35,36]. Eventually, the Co-Nb_2O_5 nanoparticles were obtained by high-temperature pyrolysis of Co-Nb-BDC precursors in air atmosphere. As a comparison, the Nb_2O_5 nanoparticles were synthesized using the same processes without Co metal ions. The X-ray diffraction (XRD) patterns of Co-Nb-BDC and Nb-BDC showed no obvious diffraction peaks, exhibiting amorphous structures of the both complexes (Fig. 1b). The bonding structure of Co-Nb-BDC precursors was identified by X-ray photoelectron spectroscopy (XPS). XPS full spectra confirmed the presence of Co characteristic peaks, suggesting the implementation of elemental introduction (Fig. S1). High-resolution C 1 s XPS spectrum further explored the occurrence of mismatched coordination reaction in Co-Nb-BDC (Fig. 1c). The Field-emission scanning electron microscopy (SEM) and transmission electron microscopy (TEM) patterns displayed both Co-Nb-BDC and Nb-BDC complexes are spherical nanoparticles with an average size of 200 nm and a uniform distribution (Fig. 1d and Fig. S2). The distribution of Nb, Co, O, and C elements was homogeneous, illustrated by the energy-dispersive X-ray (EDX) mapping patterns (Fig. S3). The colors of the Nb-BDC and Co-Nb-BDC complex powders are white and light blue, respectively, after calcining the precursor at a high temperature, the colors of obtained Co-Nb_2O_5 become light pink, indicating the different for Co-Nb-BDC compounds and Co-Nb_2O_5 compared with Nb-BDC compounds and T-Nb_2O_5 (Fig. S4 and S5).

A range of characterizations were performed to explore the structures of Nb_2O_5 and Co-Nb_2O_5 nanoparticles (Fig. 1e-l). The XRD patterns and Rietveld refinement of Nb_2O_5 and Co-Nb_2O_5 materials are displayed in Fig. 1e, f and Fig. S6. Using a Rietveld refinement, the detailed crystal structures of Nb_2O_5 and Co-Nb_2O_5 are clarified here (Fig. 1e and Fig. S6). In agreement with the experimental data, Nb elements in Co-Nb_2O_5 crystal lie in a sheet parallel to (001) and are coordinated by oxygen to form either octahedral (NbO_6) or pentagonal bipyramids (NbO_7), constituting an orthorhombic environment. The dopant occupies part of octahedral and bipyramidal sites of Nb with low coordination, lie in the denser 4 h layer of the space group *Pbam* that makes it the most stable in energy. The unique "room-and-pillar" framework with alternating layers and O-Nb polygons structure can provide a stable host for Li^+ fast transport/storage. Due to a larger ion radius of Co^{2+} (0.725 Å) than Nb^{5+} (0.69 Å), the introduction of the Co brings out a faint increase in crystallite size, accompanied by a larger unit cell volume. All the observed XRD peaks of Co-Nb_2O_5 and Nb_2O_5 can be well-indexed as an orthorhombic crystal structure with *Pbam* space group (JCPDS No. 00–027–1003), no peaks related to impurity phases (such as $CoNb_2O_5$) are observed, indicating that Co was successfully incorporated into the Nb_2O_5 lattice (Fig. 1f). Fig. S7 exhibited that the (001) D-spacing of the Co-Nb_2O_5 calculated by the Bragg equation is 3.96 Å ($2\theta = 22.44°$), higher than that of Nb_2O_5 (3.94 Å), verifying the slight expanded interlayer spacing because of the larger ionic radius Co dopants. Furthermore, T-Nb_2O_5 nanoparticles with different doping amount of Co (named as Co-Nb_2O_5-2, Co-Nb_2O_5-3 and Co-Nb_2O_5-4) were synthesized and a series of XRD tests were performed in Fig. S8. It was found that when the doping Co content exceeded 2%, impure $CoNb_2O_5$ phase was generated in the obtained materials. The inductively coupled plasma (ICP) results of Nb_2O_5, Co-Nb_2O_5, Co-Nb_2O_5-2, Co-Nb_2O_5-3, and Co-Nb_2O_5-4 (T-Nb_2O_5 doped with 0%, 2%, 3%, 5%, 10% Co, respectively) are presented in Table S1. The measured Co: Nb ratios of all samples are close to the nominal compositions. The 2% introduction amount of Co is optimal for the metal doping strategy. X-ray photoelectron spectroscopy (XPS) of Co-Nb_2O_5 and Nb_2O_5 was carried out to discuss the chemical state and effects of Co-doping. The presence of Nb and O in both samples can be observed in XPS full spectra (Fig. S9). For Nb 3d spectra in Fig. 1g, two peaks (Nb^{5+} $3d_{5/2}$ and Nb^{5+} $3d_{3/2}$) appeared due to spin-orbit coupling of Nb 3d orbital. For Co-Nb_2O_5 and Nb_2O_5, XPS peaks of Nb are located at around 207.8 and 210.6 eV, corresponding to the characteristic positions of Nb^{5+} cations [37,38]. The valence state variation is negligible due to the trace amount of Co doping. The Co spectra spectra for Co-Nb_2O_5 and Nb_2O_5 are compared in Fig. 1h, indicating that Co is successfully doped with divalent state [39,40]. All these results confirm that Nb is purely pentavalent in both cases, while Co is divalent in Co-Nb_2O_5 lattice. From the SEM and TEM images (Fig. S10 and Fig. 1i, j), both Co-Nb_2O_5 and Nb_2O_5 nanoparticles possess similar morphologies with an average diameter of 100–300 nm. High-resolution TEM (HRTEM) images exhibit that the interlayer distance of Co-Nb_2O_5 and Nb_2O_5 are 3.96 Å and 3.94 Å, respectively, which agrees well with the (001) plane of the layered structure. To explore the atomic arrangement, high-angle annular dark field STEM technique (HAADF-STEM) was used in Fig. 1k, the Co-Nb_2O_5 composes of either NbO_6 or NbO_7 to form corner sharing along [001] and edge sharing along the [100], which is well in agreement with the typical T-Nb_2O_5 phase. Finally, for Co-Nb_2O_5 particles, the uniform distribution of Nb, Co, and O elements throughout the whole particles can be observed in the EDS mapping images (Fig. 1l). In addition, the Raman spectra of Nb_2O_5 and Co-Nb_2O_5 confirm the same vibration of metal-oxygen bonds in both nanoparticles (Fig. S11). High-wavenumber band group (ν_{Hi}) (570–770 cm^{-1}) and mid-wavenumber band group (ν_{Mid}) (180–360 cm^{-1}) are illustrated in two materials [41,42]. The Brunauer–Emmett–Teller (BET) results suggest that the specific surface areas of Nb_2O_5 and Co-Nb_2O_5 were around 44.1 and 36.4 m^2 g^{-1}, respectively (Fig. S12). The pore size distribution of them was below 5 nm, which was mainly attributed to the random stacking of nanoparticles.

The electrochemical performances of Co-Nb_2O_5 and Nb_2O_5 electrodes were conducted as anode for LIBs (Fig. 2). Multiple cathodic/anodic peaks are performed by cyclic voltammetry (CV) test, which were conducted from 1.0 to 3.0 V versus Li^+/Li at a scan rate of 0.1 mV s^{-1} (Fig. S13). Because of similar open frameworks of two materials, their first three CV curves are similar and both display relatively reversible peaks. The Co-Nb_2O_5 exhibits a discharge capacity of 256.1 mAh g^{-1} and a fabulous coulombic efficiency of 98.9% at 0.1 A g^{-1} during the first electrochemical cycle, which are higher than those of Nb_2O_5 (206.7 mAh g^{-1} and 96.2%). Co-Nb_2O_5 delivers a discharge capacity of 269.0 mAh g^{-1} after 110 cycles, which is substantially higher than that of Nb_2O_5 (209.7 mAh g^{-1}) (Fig. 2a). Due to inadequate electrolyte infiltration in both Co-Nb_2O_5 and Nb_2O_5 in the initial cycle, the rate of chemical reactions lags behind charge transfer, resulting in incomplete charge/discharge processes and the capacity decreases. From the rate performance in Fig. 2b, the capacities of as-prepared Co-Nb_2O_5 electrode are obviously higher than those of T-Nb_2O_5 nanoparticles at various rates. In detail, the Co-Nb_2O_5 delivers discharge capacities of 241.8, 249.4, 234.9, 216.1, 187.9 and 141.7 mAh g^{-1} at different current densities of 0.1, 0.2, 0.5, 1, 2 and 5 A g^{-1}, respectively, while average discharge capacities of Nb_2O_5 anodes are 207.9, 205.5, 195.1, 183, 168.9 and 110.5 mAh g^{-1}. And discharge capacity of Co-Nb_2O_5 quickly recovers to 271.6 mAh g^{-1} when the current density returns to 0.1 A g^{-1}. To demonstrate the capacity retention of Co-Nb_2O_5 and Nb_2O_5 with increasing current density (based on 0.1 A g^{-1}), the capacity retain of two electrodes under different current density is compared (Table S2). The capacity retention of Co-Nb_2O_5 is consistently higher than that of Nb_2O_5, indicating the improved rate performance of Co-Nb_2O_5. The discharge/charge curves of rate performance display lower polarization and higher capacity reversibility of the Co-Nb_2O_5 compared with Nb_2O_5 (Fig. 2c and Fig. S14a). The long-term elechemical cycling stability and coulombic efficiency of Co-Nb_2O_5 and Nb_2O_5 at 1 A g^{-1} is investigated in Fig. 2d. When high current density of 1 A g^{-1} was carried out, Co-Nb_2O_5 electrodes possess higher capacity of 179.8 mAh g^{-1} and larger capacity retention of 90.0% than those of Nb_2O_5 (145.0 mAh g^{-1}, 76.7%). When areal loading is stepwise increased from 2 to 4 mg cm^{-2}, Co-Nb_2O_5 exhibits an excellent capacity retention with a capacity of 189 mAh g^{-1} (from 0.51 to 0.76 mAh cm^{-2} under 2–4 mg cm^{-2}) after 100 cycles (Fig. 2e). However, for pristine Nb_2O_5, when the mass loading increases to 4 mg cm^{-2}, the corresponding discharge capacity is only 80.2 mAh g^{-1} after 100 cycles (Fig. S15). As shown in the capacity versus current density plot and cycling life in Fig. 2f and Table S3, Co-

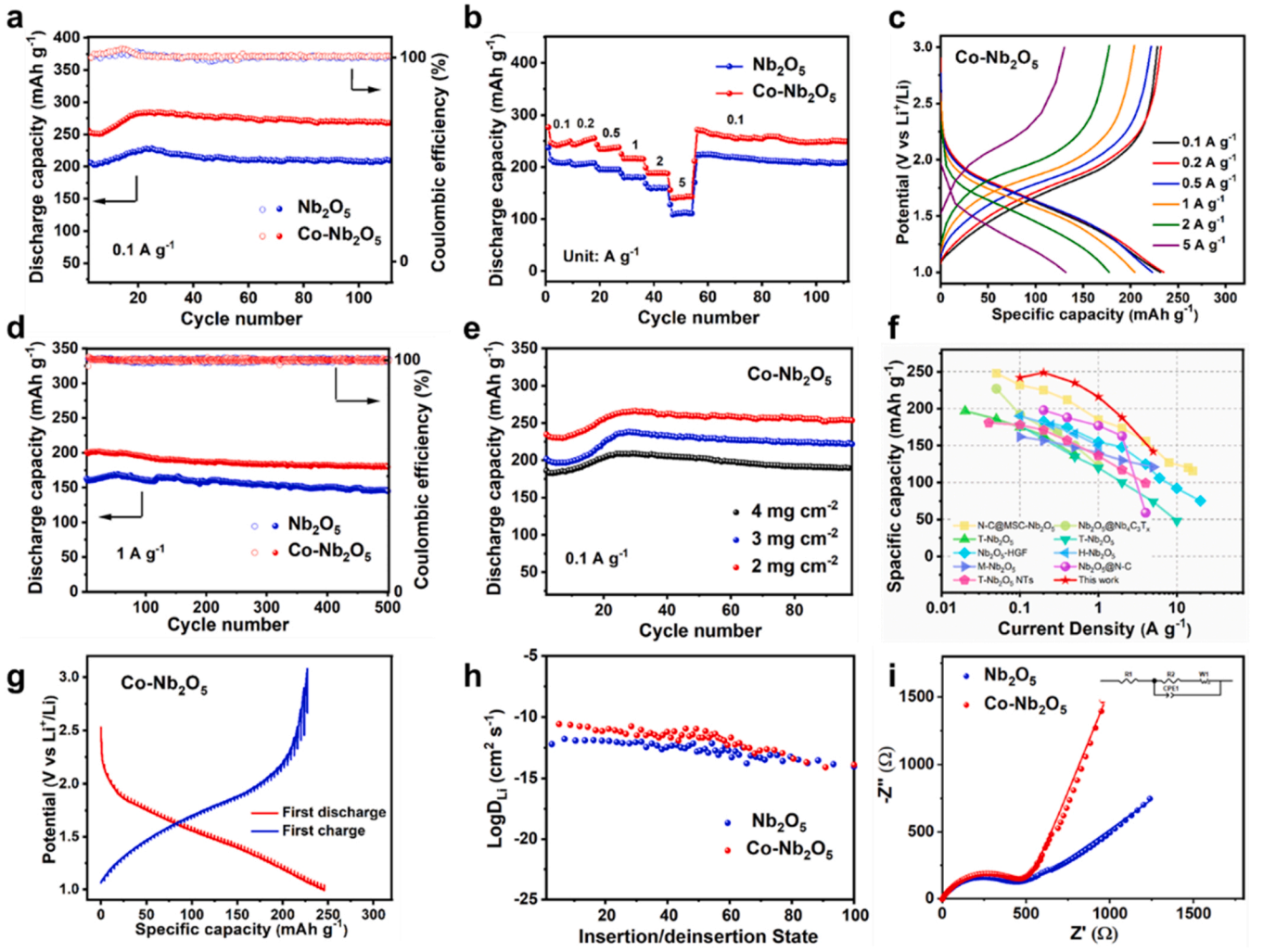

Fig. 2. Lithium storage performances of the obtained Nb_2O_5 and Co-Nb_2O_5 in 1.0–3.0 V. a) Cycling performances measured at a low current density of 0.1 A g^{-1}. b) Rate performances tested at various current densities ranging from 0.1, 0.2, 0.5, 1, 2, and 5, back to 0.1 A g^{-1}. c) The corresponding discharge/charge curves of Co-Nb_2O_5 at different rates. d) Cycling performances tested at a high current density of 1 A g^{-1}. e) Cycling performance of Co-Nb_2O_5 with high areal loadings of 2, 3 and 4 mg cm^{-2} at 0.1 A g^{-1}. f) The comparison of specific capacities of Co-Nb_2O_5 at various current densities with results of other reported niobium pentoxide materials. g) The GITT curves of charge/discharge process for Co-Nb_2O_5. h) The calculated chemical diffusion coefficient for Li^+ in Nb_2O_5 and Co-Nb_2O_5. i) Comparison of EIS spectra of Nb_2O_5 and Co-Nb_2O_5 samples.

Nb_2O_5 exhibited much higher capacities than most type of Nb_2O_5-based composite materials at various current densities [14,24,43–49]. Galvanostatic intermittent titration technique (GITT) date was collected to estimate the theoretical capacity of Co-Nb_2O_5 and Nb_2O_5 eletrodes (Fig. 2g and Fig. S14 b). The theoretical initial discharge specific capacities of Co-Nb_2O_5 and Nb_2O_5 are 201.8 and 245.6 mA h g^{-1}, respectively. The Li^+ diffusion coefficients of Co-Nb_2O_5 are calculated to be about 2.1 × 10^{-12} cm^2 s^{-1}, about one order of magnitude higher than those of Nb_2O_5 (2.0 × 10^{-13} cm^2 s^{-1}) (Fig. 2h). The electrochemical impedance spectroscopy (EIS) plot and fitted results indicates a lower charge-transfer resistance and faster diffusion resistance of Co-Nb_2O_5 anode compared with Nb_2O_5 electrode, mostly owing to the expanded interlayer structure and enhanced electron conductivity (Fig. 2i and Fig. S16). The Co-Nb_2O_5 electrode displays smaller Warburg coefficients ($\sigma = 160.0$) than those of the Nb_2O_5 electrode ($\sigma = 236.5$), and larger Li^+ diffusion coefficients (8.5 × 10^{-12} cm^2 s^{-1}) than Nb_2O_5 (2.89 × 10^{-13} cm^2 s^{-1}), which further proves better diffusion kinetics of Li^+ after trace Co doping (Fig. S16). SEM, TEM and HRTEM results of Co-Nb_2O_5 after 100 cycles are shown in Fig. S17. The nanoparticles maintain at an average size of 200 nm and a uniform distribution, indicating good structure stability of the Co-Nb_2O_5 after undergoing electrochemical cycling. HRTEM results display that the electrode material still exhibits good crystallinity after cycling, further indicating the cycling stability. Co-Nb_2O_5 as an anode material for LIBs show higher reversible capacity and better rate capability compared with Nb_2O_5 materials, which is ascribed to the faster diffusion coefficient induced by the enlarged interlayer spacing and improved electrical conductivity.

To better investigate lithium storage mechanism in Co-Nb_2O_5, in situ XRD was used to unveil the structural evolution during charge/discharge processes (Fig. 3) [50–54]. The high-quality and clear XRD curves were shown during several original charge/discharge processes (Fig. 3a and c). Major diffraction peaks of Co-Nb_2O_5 and Nb_2O_5 were covered in the selected 2θ region (20°−40°). Co-Nb_2O_5 displayed three similar main peaks at 22.4°, 28.3° and 36.6°, while Nb_2O_5 showed diffraction peaks at 22.6°, 28.4° and 36.6°, respectively corresponding to the planes of (001), (180) and (200). Both Nb_2O_5 and Co-Nb_2O_5 show one-phase solid solution reactions during lithium insertion/extraction processes according to the reversible shift of characteristic diffraction peaks without new peaks. When discharging from open-circuit voltage (about 2.5 V) back to 1.0 V, the interlayer (001) plane of Nb_2O_5 gradually shifts toward low angle (from 22.6° to 21.9°), which are attributed to the constriction of the a-b plane and the expansion of the lattice

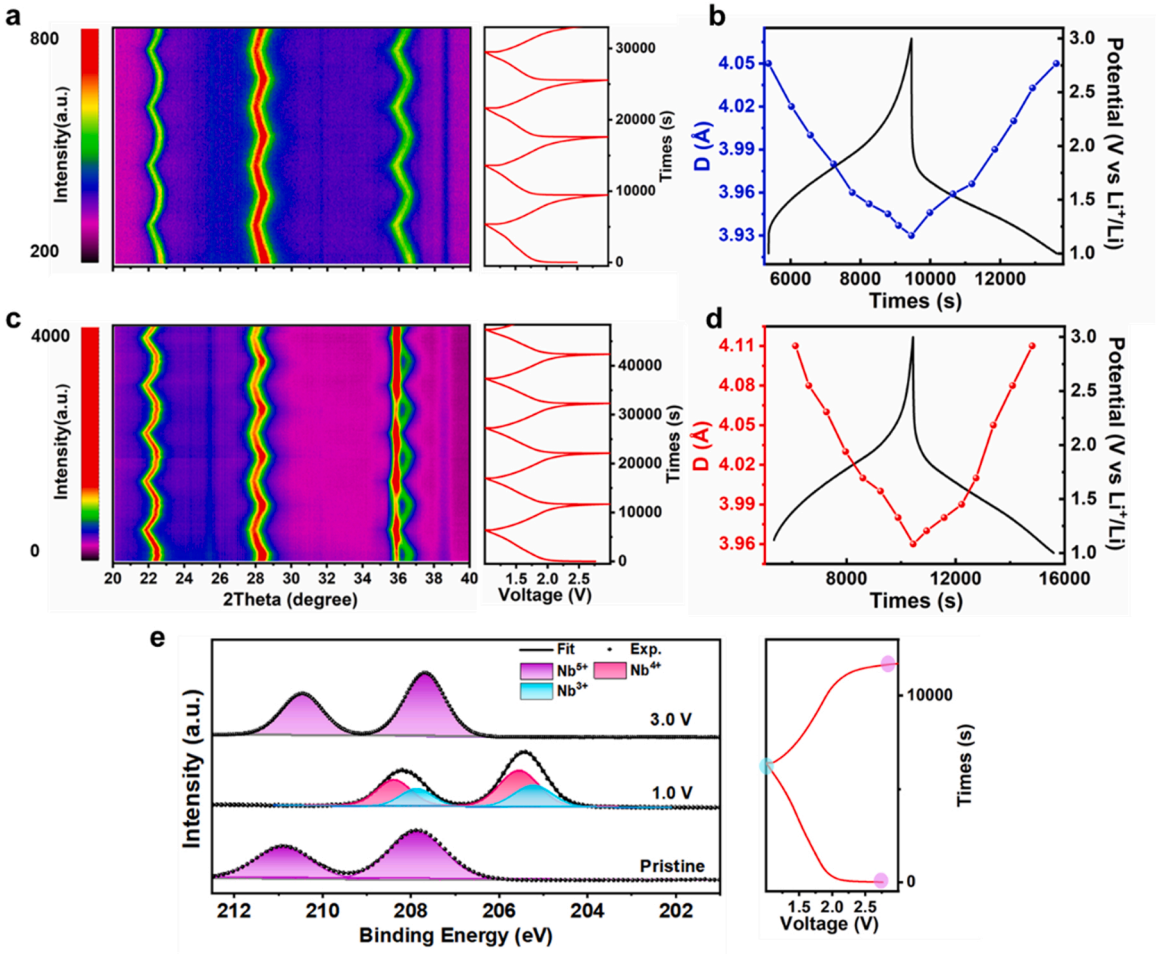

Fig. 3. *In situ* XRD patterns of a) Nb_2O_5 and c) Co-Nb_2O_5 samples during galvanostatic charge and discharge at 0.1 A g^{-1}. The horizontal axis represents the selected 2θ regions from 20° – 40°, and time is plotted on the vertical axis. The corresponding voltage curves plotted to the right. The diffraction intensity is color-coded according to the scale bar in the left. The interlayer spacing (D) evolution of (001) plane in b) Nb_2O_5 and d) Co-Nb_2O_5 samples during galvanostatic charge and discharge at 0.1 A g^{-1}. e) High-resolution XPS spectra of the Co-Nb_2O_5 electrodes upon lithiation/delithiation processes. The corresponding voltage profile is shown on the right. The potentials of the ex situ samples are marked by colored circles.

spacings after Li-insertion, accompanied with the formation of $Li_xNb_2O_5$. In contrast, during the charging process, these three typical diffraction peaks gradually recovered to high angles with the extraction of Lithium. *In situ* XRD analysis of Co-Nb_2O_5 electrodes (Fig. 3c) revealed generally the same trend as that of the comparison sample (Nb_2O_5). On the basis of the Bragg equation, the varition of interlayer (001) plane in Co-Nb_2O_5 was 4.11–3.96 Å, and the increment rate was 3.79%, which was larger than that of Nb_2O_5 (3.05%, from 3.93 to 4.05 Å), illustrating increased lithium storage sites and higher discharging capacity. From in situ XRD (Fig. S18), the relative varition of interlayer (001) plane in both Co-Nb_2O_5 and Nb_2O_5 are consistent with the results in Fig. 3a. To further analyze the electrochemical kinetics during charge/discharge processes, *ex-situ* EIS results were shown in Fig. S19. As the Co-Nb_2O_5 electrode discharging from pristine status to 2.0 V, and further discharging to 1.0 V during the initial cycle, no significant changes of resistances is observed. When the battery was gradually recharged to 3.0 V, the resistance returns closely to the initial value, indicating high stabilization of Li^+ intercalation process for Co-Nb_2O_5 electrode. Furthermore, XPS analysis was performed on cycled Co-Nb_2O_5 and Nb_2O_5 electrodes at fully discharged and charged states, as shown in Fig. 3e, Fig. S20, and Fig. S21. For pristine Co-Nb_2O_5, the oxidation of Nb is + 5. When discharged to 1.0 V, new double peaks are obtained at 208.58/205.78 eV and 208.08/205.38 eV, lower binding energies can be well fitted by the characteristic peaks of Nb^{4+} and Nb^{3+} respectively [55,56]. When charged to 3.0 V, the Nb 3d peaks located at 210.98 eV and 208.29 eV corresponding to Nb^{5+} $3d_{5/2}$ and Nb^{5+} $3d_{3/2}$. XPS results show that the capacity of Co-Nb_2O_5 is attributed to the Nb^{5+}/Nb^{4+} and Nb^{4+}/Nb^{3+} redox couples during charge/discharge process. And the valence state of Nb completely returns to + 5 after charging to 3.0 V. By comparison, the pure Nb_2O_5 displays lower theoretical capacities due to a one-electron redox couple of Nb^{5+}/Nb^{4+} (Fig S20) [19,57]. From high-resolution XPS spectra of Co 2p (Fig S21), the sample presents one major peak centered at 781.2 eV at open circuit, implying the typical Co $2p_{3/2}$ of Co_3O_4. Upon discharging to 1.0 V, the Co 2p peak was shifted to 779.5 eV, consistent with the reduction to Co^{2+}. After charging back to 3.0 V, the Co-Nb_2O_5 electrode returned to Co_3O_4. For only trace Co is doped (5%), the capacity contribution of Co redox in Co-Nb_2O_5 electrode is negligible. The in situ XRD and *ex situ* XPS techniques indicated the deintercalation reaction mechanism, larger variation of interlayer plane, and multiple redox couples of Nb^{5+}/Nb^{4+} and Nb^{4+}/Nb^{3+}, which endowed the Co-Nb_2O_5 with higher lithium storage capacity and better rate performance.

To deeply elucidate the electrical conductivity, reaction mechanism based on experimental results and identify the roles of Co metal dopants, I-V tests, UV–vis spectra and density functional theory (DFT) calculation was conducted (Fig. 4). Electrical conductivity is a key factor that affects polarization of electrodes, I-V tests are measured to investigate the electrical transport of T-Nb_2O_5 and Co-Nb_2O_5 (Fig. 4a). The Co-Nb_2O_5 delivers a lower resistance than Nb_2O_5, which correlates with higher electron conductivity. The characteristics of both electrodes deliver

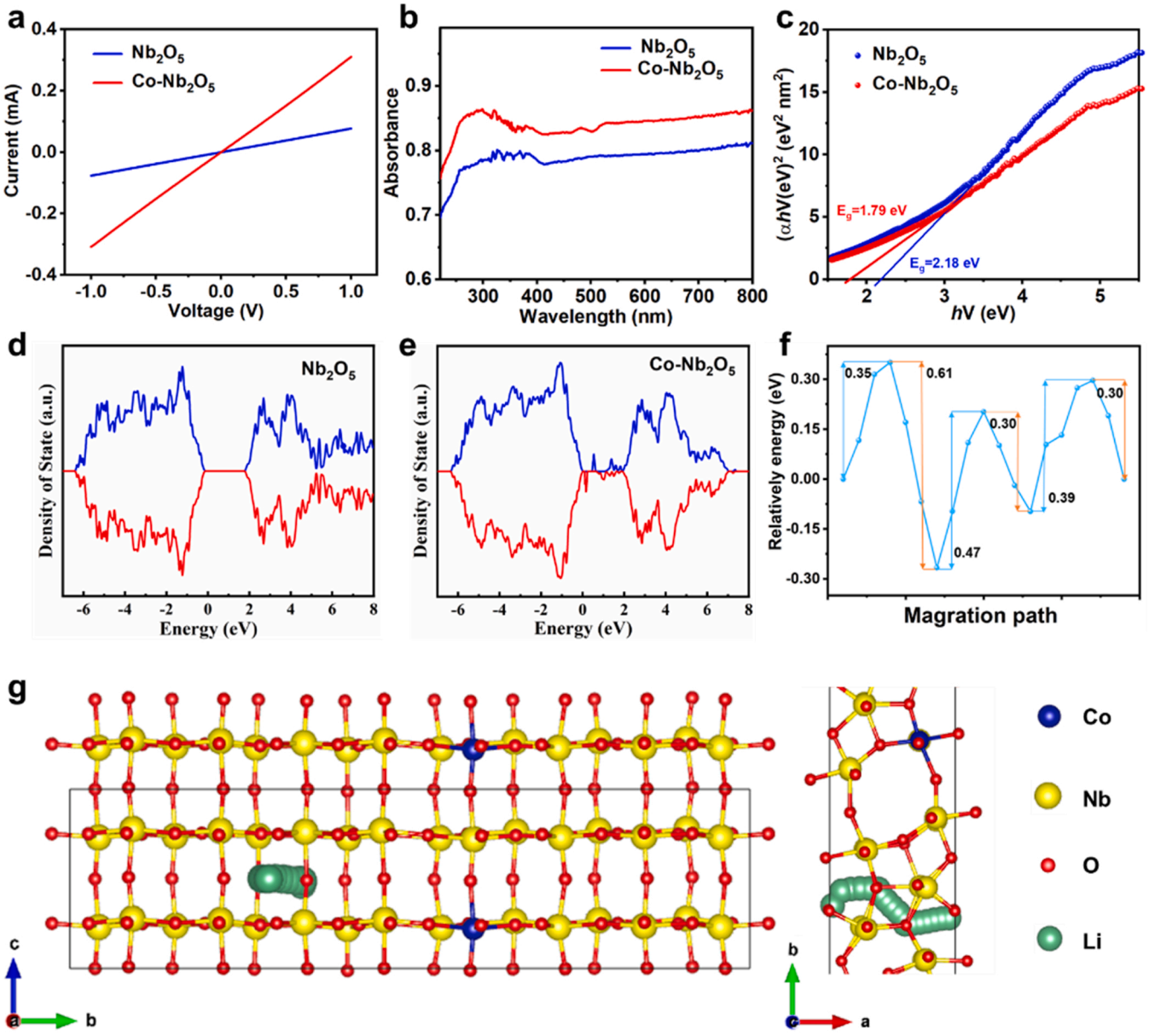

Fig. 4. a) I-V characteristics of Nb_2O_5 and Co-Nb_2O_5 nanoparticles. b) UV−vis diffuse reflectance spectra, c) photon energy vs $(\alpha hv)^2$ curves of Nb_2O_5 and Co-Nb_2O_5 nanoparticles. d, e) Partial density of states of Co-Nb_2O_5 and pristine T-Nb_2O_5. f) The migration energy profiles of Co-Nb_2O_5. g) Simulated Li^+ migration paths viewed from different lattice planes of Co-Nb_2O_5. The rectangular boxes represent the Li^+ migration regions near the highest energy barrier.

ohmic behavior, and the calculated conductivity of T-Nb_2O_5 and Co-Nb_2O_5 are 3.15×10^{-3} and 4.02×10^{-2}, respectively. These results confirmed that the electron conductivity is increased by trace Co doping strategy, and Co-Nb_2O_5 is effectively changes from semiconductor to metallic behavior. The UV–vis spectra are displayed to better confirm the influence on electron conductivity after doping trace Co (Fig. 4b). The Co-Nb_2O_5 electrode performs stronger absorption within the wavelength range of 250 − 500 nm than Nb_2O_5. Furthermore, the corresponding bandgap of Co-Nb_2O_5 is 1.79 eV, lower than that of Nb_2O_5 (2.18 eV) (Fig. 4c), indicating the enhancement of intrinsic electron conductivity by trace Co doping. Partial density of states (PDOS) was used to explore electron conductivity of Co doped Nb_2O_5 and the pristine T-Nb_2O_5 in Fig. 4d, e. The comparative sample Nb_2O_5 displayed a semiconducting behavior for the wide band gap between valence and conduction bands (1.8 eV). As shown in Fig. 4d, spin-up defect states near the Fermi levels for Co-Nb_2O_5 were introduced, which can be attributed to the Co doping. The doped Co as the donors, resulting in the construction of impurity bands at the Fermi level and ultimately a huge narrowing of band gap. The semiconductor to metal transition was therefore realized by Co doping, as evidenced by the improved electrical conductivity of Co-Nb_2O_5. Due to the solid solution reaction mechanism of Co-Nb_2O_5, the lithium ions diffusion pathways follow a quasi-2D network during charge/discharge process, which is similar to the non-doped compound. As relatively shorter Co-O band distance compared with Nb-O distances in Co-Nb_2O_5, the shift of lithium ions is preferably away from the Co dopant sites in the structure to accommodate more Li, the most practicable migration path for lithium ions in Co-Nb_2O_5 is illustrated in Fig. 4g. The corresponding free energy diagram for Li migration along an armchair trajectory can be calculated out (Fig. 4f). The highest migration energy value of Co-Nb_2O_5 is 0.47 eV, which is almost the same as that of T-Nb_2O_5 obtained by previous work [14]. The Li ion diffusion channels, diffusion paths and the intrinsic ionic conductivity of Co-Nb_2O_5 are similar to those of pure T-Nb_2O_5. The introduction of Co dopant can effectively improve the electronic conductivity

while maintain the original excellent ionic conductivity, which further promotes the transport kinetics of Li in Co-Nb_2O_5, which agrees well with experimental results. Moreover, the small difference among lithium migration energies (about 0.12 eV) displays the efficiently locations for lithium storage, which is coincided with smooth sloping capacity-voltage curves upon Li^+ intercalation/deintercalation processes.

To validate the potential for practical applications, full batteries were constructed using commercial $LiFePO_4$ and prepared Co-Nb_2O_5 to evaluate the electrochemical performance, as shown in the schematic in Fig. 5a. The discharge/charge curves of $LiFePO_4$ and Co-Nb_2O_5 shows the average 1.6 V voltage difference between them and an operating voltage of 1.0–2.5 V was chosen for the full cell (Fig. 5b). In the $LiFePO_4$/ Co-Nb_2O_5 full cell, the capacity of cathode was 1.1–1.2 times that of anode, the discharge capacity was calculated according to Co-Nb_2O_5 anode. A reversible discharge capacity of 229.8 mAh g^{-1} is obtained in the full battery at 0.1 A g^{-1} and it maintained 208.3 mAh g^{-1} after 100 cycles, indicating high capability (Fig. 5c). The rate performances of $LiFePO_4$/Co-Nb_2O_5 full cell are shown in Fig. 5d and e, the specific discharge capacities 225.9, 184.3, 151.4, 126.8, 109.4, and 90.8 mA h g^{-1} were obtained at 0.1, 0.2, 0.3, 0.5, 1, and 2 A g^{-1}, respectively. The capacity reversibly recovers to 215.2 mAh g^{-1} when the rate skips back to 0.1 A g^{-1}. The results reveal that $LiFePO_4$/Co-Nb_2O_5 full battery displays a satisfactory rate capability for fast-charging application. Moreover, the full cell exhibits long cycling life, with the discharge capacity retention of 158.1 mA h g^{-1} at 0.2 A g^{-1} after 1000 cycles, yielding an average capacity decay rate of 0.18% per cycle, as shown in Fig. 5f. Furthermore, a single $LiFePO_4$/Co-Nb_2O_5 full battery shows a high open-circuit potential of about 2.7 V, and two batteries connected in series can light up a LED light band in parallel, indicating its practical application (Fig. 5g).

3. Conclusion

The introduction of trace Co dopants into insertion-type T-Nb_2O_5 is well demonstrated as a promising strategy to improve the intrinsic electric conductivity and induce multielectron redox of Nb^{5+}/Nb^{4+} and Nb^{4+}/Nb^{3+}, achieving ultrafast lithium storage and high-capacity. The trace Co dopants partially replace original Nb sites with low coordination, which enhance the metallic character and multielectron redox of T-Nb_2O_5, meanwhile maintain the advantages of the crystalline host structure. Incorporated with various experimental measurements such as in situ XRD, *ex situ* XPS analysis and DFT calculations, the excellent fast-charging and high-capacity of Co-Nb_2O_5 is due to its high electron

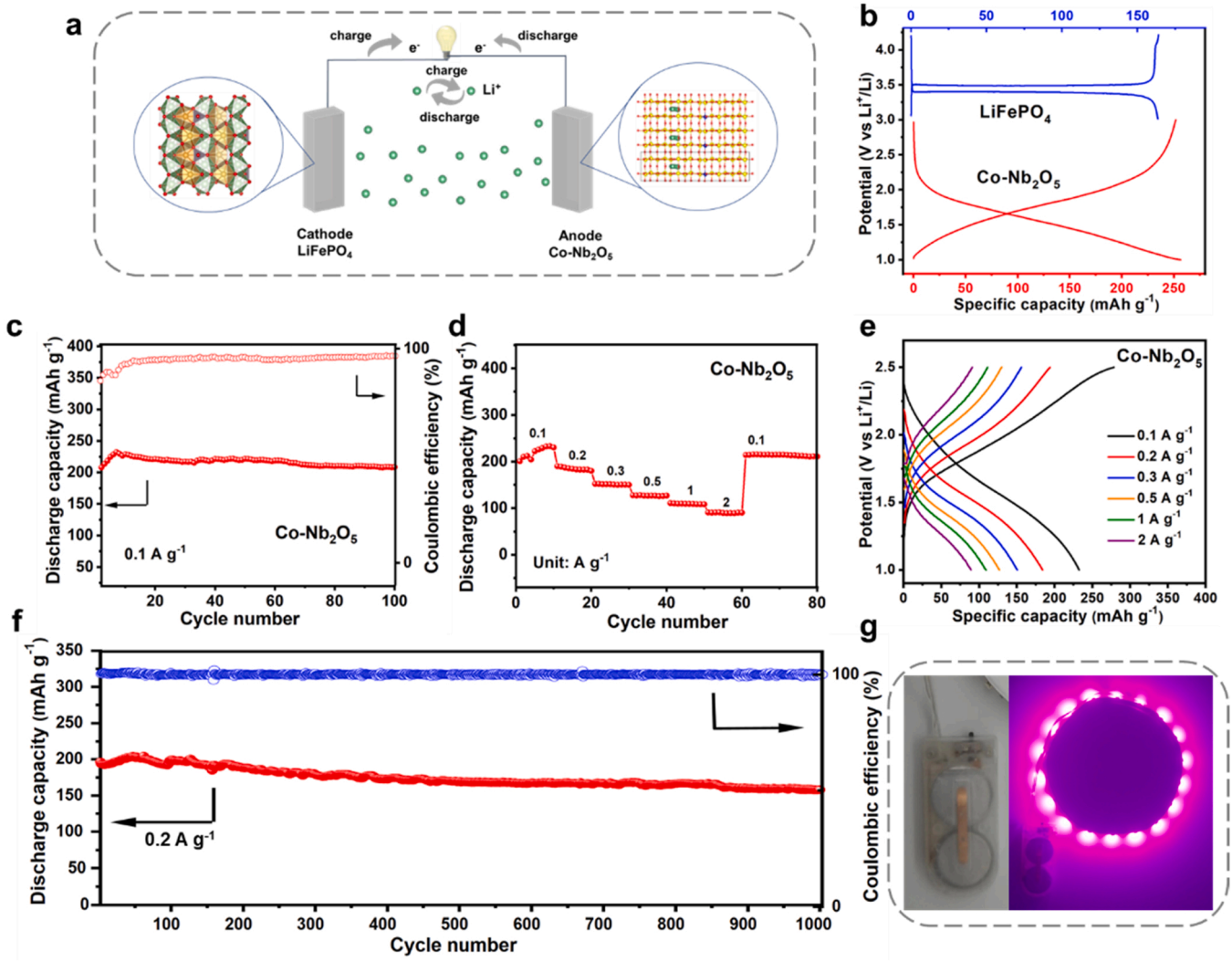

Fig. 5. a) Schematic illustration of the fast charging/discharging full cell with Co-Nb_2O_5 as the anode and $LiFePO_4$ as the cathode. b) Galvanostatic charge/discharge (GCD) curves of the cathode and anode to show the operating voltage for the full cell. c) Cycling performance and the corresponding Coulombic efficiencies tested at 0.1 A g^{-1}. Rate performance (d) conducted at 0.1, 0.2, 0.3, 0.4, and 0.5 A g^{-1} and the corresponding discharge/charge curves at different rates (e). f) Long-term cycling stability of the full cell at 0.2 A g^{-1}. g) Digital images show that two batteries could light a LED light band in parallel.

conductivity and redox chemistry upon lithium insertion. Moreover, Co-Nb_2O_5 also exhibits outstanding rate performance, high-capacity and long cycling life as a anode in Li-ion full batteries. Considering the ultrafast lithium storage and high-capacity of our Co-Nb_2O_5 nanoparticles, the introduction of transition metal dopants into insertion-type materials offers a new idea for fast-charging LIBs.

CRediT authorship contribution statement

J.H. Chen and J.S. Meng contributed equally to this work. J.H. Chen designed the experiments and performed the data analyses as well as wrote the manuscript. J.S. Meng guided the experimental design ideas of the manuscript. K. Han carried out in-situ XRD tests. F. Liu carried out TEM abalysis and W.X. Wang draw the schematic diagram. J.S. Meng and Q.Y. An contributed to the conception of the study and revised the manuscript. Q.Y. An and L.Q. Mai were in charge of this scientific research project, and the leaders of actual coordination of contributions.

Declaration of Competing Interest

The authors declare that they have no known competing financial interests or personal relationships that could have appeared to influence the work reported in this paper.

Data Availability

Data will be made available on request.

Acknowledgements

This work was supported by the Key Program of Hainan Province (Grant No. 2021CXLH0007), the National Science Foundation of China through Projects (Grant No. 52103329), the Sanya Open Foundation of Science and Technology Park of Wuhan University of Technology (Grant No. 0000409), the Sanya Open Foundation of Science and Technology Park of Wuhan University of Technology (Grant No. 0000419), and the Natural Science Foundation of Hainan Province, China (Grant No. SCX2022035).

Appendix A. Supporting information

Supplementary data associated with this article can be found in the online version at doi:10.1016/j.nanoen.2023.108377.

References

[1] Y. Liu, Y. Zhu, Y. Cui, Challenges and opportunities towards fast-charging battery materials, Nat. Energy 4 (2019) 540–550.
[2] L. Mai, M. Yan, Y. Zhao, Track batteries degrading in real time, Nature 546 (2017) 469–470.
[3] N.-S. Choi, Z. Chen, S.A. Freunberger, X. Ji, Y.-K. Sun, K. Amine, G. Yushin, L. F. Nazar, J. Cho, P.G. Bruce, Challenges facing lithium batteries and electrical double-layer capacitors, Angew. Chem. Int. Ed. 51 (2012) 9994–10024.
[4] Z. Liu, W. Dong, J. Wang, C. Dong, Y. Lin, I.W. Chen, F. Huang, Orthorhombic Nb_2O_{5-x} for durable high-rate anode of Li-ion batteries, iScience 23 (2020), 100767.
[5] J. Deng, C. Bae, A. Denlinger, T. Miller, Electric vehicles batteries: requirements and challenges, Joule 4 (2020) 511–515.
[6] N. Loeffler, D. Bresser, S. Passerini, M. Copley, Secondary Lithium-ion battery anodes: from first commercial batteries to recent research activities, Johnson Matthey, Technol. Rev. 59 (2015) 34–44.
[7] Y. Guo, Z. Wang, X. Lu, J. Lu, K. Rabia, H. Chen, R. Hu, H. Tang, Q. Zhang, Z. Li, Core-shell ZnO@ C: N hybrids derived from MOFs as long-cycling anodes for lithium ion batteries, Chem. Commun. 56 (2020) 1980–1983.
[8] H. Chen, R. Liu, Y. Wu, J. Cao, J. Chen, Y. Hou, Y. Guo, R. Khatoon, L. Chen, Q. Zhang, Q. He, J. Lu, Interface coupling 2D/2D $SnSe_2$/graphene heterostructure as long-cycle anode for all-climate lithium-ion battery, Chem. Eng. J. 407 (2021), 126973.
[9] Z. Zhao, K. Xia, Y. Hou, Q. Zhang, Z. Ye, J. Lu, Designing flexible, smart and self-sustainable supercapacitors for portable/wearable electronics: from conductive polymers, Chem. Soc. Rev. 50 (2021) 12702–12743.
[10] D. Bresser, K. Hosoi, D. Howell, H. Li, H. Zeisel, K. Amine, S. Passerini, Perspectives of automotive battery R&D in China, Germany, Japan, and the USA, J. Power Sources 382 (2018) 176–178.
[11] Z. Liu, W. Dong, J. Wang, C. Dong, Y. Lin, I.W. Chen, F. Huang, Orthorhombic Nb_2O_{5-x} for durable high-rate anode of Li-ion batteries, iScience 23 (2020), 100767.
[12] P.F. Yu, C.L. Li, X.X. Guo, Sodium storage and pseudocapacitive charge in textured $Li_4Ti_5O_{12}$ thin films, J. Phys. Chem. C. 118 (2014) 10616–10624.
[13] D. Chen, J.H. Wang, T.F. Chou, B. Zhao, M.A. El-Sayed, M. Liu, Unraveling the nature of anomalously fast energy storage in T-Nb_2O_5, J. Am. Chem. Soc. 139 (2017) 7071–7081.
[14] J. Meng, Q. He, L. Xu, X. Zhang, F. Liu, X. Wang, Q. Li, X. Xu, G. Zhang, C. Niu, Z. Xiao, Z. Liu, Z. Zhu, Y. Zhao, L. Mai, Identification of phase control of carbon-confined Nb_2O_5 nanoparticles toward high-performance lithium storage, Adv. Energy Mater. 9 (2019), 1802695.
[15] V. Augustyn, J. Come, M.A. Lowe, J.W. Kim, P.L. Taberna, S.H. Tolbert, H. D. Abruna, P. Simon, B. Dunn, High-rate electrochemical energy storage through Li^+ intercalation pseudocapacitanc, Nat. Mater. 12 (2013) 518–522.
[16] L. Yan, G. Chen, M. Zhou, H. Luo, Oxygen-deficient niobium oxide in carbon matrix as anode for lithium-ion battery, ECS Trans. 66 (2015) 277.
[17] X. Wang, Q. Li, L. Zhang, Z. Hu, L. Yu, T. Jiang, C. Lu, C. Yan, J. Sun, Z. Liu, Caging Nb_2O_5 nanowires in PECVD-derived graphene capsules toward bendable sodium-ion hybrid supercapacitors, Adv. Mater. 30 (2018), 1800963.
[18] Z. Tong, R. Yang, S. Wu, D. Shen, T. Jiao, K. Zhang, W. Zhang, C.S. Lee, Surface-engineered black niobium oxide@graphene nanosheets for high-performance sodium-/potassium-ion full batteries, Small 15 (2019), 1901272.
[19] J.Y. Cheong, C. Kim, J.W. Jung, K.R. Yoon, S.H. Cho, D.Y. Youn, H.Y. Jang, I. D. Kim, Formation of a surficial bifunctional nanolayer on Nb_2O_5 for ultrastable electrodes for lithium-ion battery, Small 13 (2017), 1603610.
[20] S.J. Deng, H. Zhu, G.Z. Wang, M. Luo, S.H. Shen, C.Z. Ai, L. Yang, S.W. Lin, Q. H. Zhang, L. Gu, B. Liu, Y. Zhang, Q. Liu, G.X. Pan, Q.Q. Xiong, X.L. Wang, X. H. Xia, J.P. Tu, Boosting fast energy storage by synergistic engineering of carbon and deficiency, Nat. Commun. 11 (2020) 132.
[21] H.T. Sun, L. Mei, J.F. Liang, Z.P. Zhao, C. Lee, H.L. Fei, M.N. Ding, J. Lau, M.F. Li, C. Wang, X. Xu, G.L. Hao, B. Papandrea, I. Shakir, B. Dunn, Y. Huang, X.F. Duan, Three-dimensional holey-graphene/niobia composite architectures for ultrahigh-rate energy storage, Science 356 (2017) 599–604.
[22] Z. Song, H. Li, W. Liu, H. Zhang, J. Yan, Y. Tang, J. Huang, H. Zhang, X. Li, Ultrafast and stable Li-(de)intercalation in a large single crystal H-Nb_2O_5 anode via optimizing the homogeneity of electron and ion transport, Adv. Mater. 32 (2020), 20201001.
[23] J.G. Weissman, E.I. Ko, P. Wynblatt, J.M. Howe, High-resolution electron microscopy and image simulation of TT-, T-, and H-niobia and model silica-supported niobium surface oxides, Chem. Mater. 1 (1989) 187–193.
[24] K.J. Griffith, A.C. Forse, J.M. Griffin, C.P. Grey, High-rate intercalation without nanostructuring in metastable Nb_2O_5 bronze phases, J. Am. Chem. Soc. 138 (2016) 8888–8899.
[25] F. Liu, X. Cheng, R. Xu, Y. Wu, Y. Jiang, Y. Yu, Binding sulfur-doped Nb_2O_5 hollow nanospheres on sulfur-doped graphene networks for highly reversible sodium storage, Adv. Funct. Mater. 28 (2018), 1800394.
[26] Y. Ma, Y. Ma, G. Giuli, H. Euchner, A. Groß, G.O. Lepore, F. d'Acapito, D. Geiger, J. Biskupek, U. Kaiser, H.M. Schütz, A. Carlsson, T. Diemant, R.J. Behm, M. Kuenzel, S. Passerini, D. Bresser, Introducing highly redox-active atomic centers into insertion-type electrodes for lithium-ion batteries, Adv. Energy Mater. 10 (2020), 2000783.
[27] S.S. Qian, H.X. Yu, X. Cheng, R.T. Zheng, H.J. Zhu, T.T. Liu, M. Shui, Y. Xie, J. Shu, Rapid and durable electrochemical storage behavior enabled by $V_4Nb_{18}O_{55}$ beaded nanofibers: a joint theoretical and experimental study, J. Mater. Chem. A 6 (2018) 17389–17400.
[28] C. Yang, S. Yu, C.F. Lin, F. Lv, S.Q. Wu, Y. Yang, W. Wang, Z.Z. Zhu, J.B. Li, N. Wang, S.J. Guo, $Cr_{0.5}Nb_{24.5}O_{62}$ nanowires with high electronic conductivity for high-rate and long-life lithium-ion storage, ACS Nano 11 (2017) 4217–4224.
[29] C. Yang, Y.L. Zhang, F. Lv, C.F. Lin, Y. Liu, K. Wang, J.R. Feng, X.H. Wang, Y. J. Chen, J.B. Li, S.J. Guo, Porous $ZrNb_{24}O_{62}$ nanowires with pseudocapacitive behavior achieve high-performance lithium-ion storage, J. Mater. Chem. A 5 (2017) 22297–222304.
[30] H. Yu, H. Lan, L. Yan, S. Qian, X. Cheng, H. Zhu, N. Long, M. Shui, J. Shu, $TiNb_2O_7$ hollow nanofiber anode with superior electrochemical performance in rechargeable lithium ion batteries, Nano Energy 38 (2017) 109–117.
[31] Y. Yang, H. Zhu, J. Xiao, H. Geng, Y. Zhang, J. Zhao, G. Li, X.L. Wang, C.C. Li, Q. Liu, Achieving ultrahigh-rate and high-safety Li^+ storage based on interconnected tunnel structure in micro-size niobium tungsten oxides, Adv. Mater. 32 (2020), 1905295.
[32] M.A. Aegerter, Sol–gel niobium pentoxide: a promising material for electrochromic coatings, batteries, nanocrystalline solar cells and catalysis, Sol. Energy Mater. Sol. Cells 68 (2001) 401–422.
[33] R.L. Hou, B. Liu, Y.L. Sun, L.Y. Liu, J.N. Meng, M.D. Levi, H.X. Ji, X.B. Yan, Recent advances in dual-carbon based electrochemical energy storage devices, Nano Energy 72 (2020), 104728.
[34] Q. Deng, Y. Fu, C. Zhu, Y. Yu, Niobium-based oxides toward advanced electrochemical energy storage: recent advances and challenges, Small 15 (2019), 1804884.
[35] J. Meng, X. Liu, C. Niu, Q. Pang, J. Li, F. Liu, Z. Liu, L. Mai, Advances in metal–organic framework coatings: versatile synthesis and broad applications, Chem. Soc. Rev. 49 (2020) 3142–3186.

[36] Q. Li, W. Zhang, J. Peng, W. Zhang, Z. Liang, J. Wu, J. Feng, H. Li, S. Huang, Metal-organic framework derived ultrafine Sb@porous carbon octahedron via in situ substitution for high-performance sodium-ion batteries, ACS Nano 9 (2021) 15104–15113.

[37] D. Sarama, C. Rao, XPES studies of oxides of second- and third-row transition metals including rare earths, J. Electron Spectrosc. Relat. Phenom. 20 (1980) 25–45.

[38] H.D. Asfaw, C.-W. Tai, L. Nyholm, K. Edström, Over-stoichiometric NbO_2 nanoparticles for a high energy and power density lithium microbattery, ChemNanoMat 3 (2017) 646–655.

[39] X. Wang, J.Q. Meng, M. Wang, Y. Xiao, R. Liu, Y. Xia, Y. Yao, E. Metwalli, Q. Zhang, B. Qiu, Z. Liu, J. Pan, L.D. Sun, C.H. Y an, P. Muller-Buschbaum, Y. J. Cheng, Facile scalable synthesis of TiO_2/carbon nanohybrids with ultrasmall TiO_2 nanoparticles homogeneously embedded in carbon matrix, ACS Appl. Mater. Interfaces 7 (2015) 24247–24255.

[40] L. Zheng, X. Wang, Y. Xia, S. Xia, E. Metwalli, B. Qiu, Q. Ji, S. Yin, S. Xie, K. Fang, S. Liang, M. Wang, X. Zuo, Y. Xiao, Z. Liu, J. Zhu, P. Muller-Buschbaum, Y. J. Cheng, Scalable in situ synthesis of $Li_4Ti_5O_{12}$/carbon nanohybrid with supersmall $Li_4Ti_5O_{12}$ nanoparticles homogeneously embedded in carbon matrix, ACS Appl. Mater. Interfaces 10 (2018) 2591–2602.

[41] B. Lu, T.J. Smart, D. Qin, J.E. Lu, N. Wang, L. Chen, Y. Peng, Y. Ping, S. Chen, Nitrogen and iron-codoped carbon hollow nanotubules as high-performance catalysts toward oxygen reduction reaction: a combined experimental and theoretical study, Chem. Mater. 29 (2017) 5617–5628.

[42] W. Yang, X. Liu, X. Yue, J. Jia, S. Guo, Bamboo-like carbon nanotube/Fe_3C nanoparticle hybrids and their highly efficient catalysis for oxygen reduction, J. Am. Chem. Soc. 137 (2015) 1436–1439.

[43] C.J. Zhang, S.J. Kim, M. Ghidiu, M.-Q. Zhao, M.W. Barsoum, V. Nicolosi, Y. Gogotsi, Layered orthorhombic Nb2O5@$Nb_4C_3T_x$ and TiO_2@$Ti_3C_2T_x$ hierarchical composites for high performance Li-ion batteries, Adv. Funct. Mater. 26 (2016) 4143–4151.

[44] H. Zhang, Y. Wang, P. Liu, S.L. Chou, J.Z. Wang, H. Liu, G. Wang, H. Zhao, Highly ordered single crystalline nanowire array assembled three-dimensional $Nb_3O_7(OH)$ and Nb_2O_5 superstructures for energy storage and conversion applications, ACS Nano 10 (2016) 507–514.

[45] M. Lübke, A. Sumboja, I.D. Johnson, D.J.L. Brett, P.R. Shearing, Z. Liu, J.A. Darr, High power nano-Nb_2O_5 negative electrodes for lithium-ion batteries, Electrochim. Acta 192 (2016) 363–369.

[46] S. Li, T. Wang, W. Zhu, J. Lian, Y. Huang, Y.-Y. Yu, J. Qiu, Y. Zhao, Y.-C. Yong, H. Li, Controllable synthesis of uniform mesoporous H-Nb_2O_5/rGO nanocomposites for advanced lithium ion hybrid supercapacitors, J. Mater. Chem. A 7 (2019) 693–703.

[47] Z. Hu, Q. He, Z. Liu, X. Liu, M. Qin, B. Wen, W. Shi, Y. Zhao, Q. Li, L. Mai, Facile formation of tetragonal-Nb_2O_5 microspheres for high-rate and stable lithium storage with high areal capacity, Sci. Bull. 65 (2020) 1154–1162.

[48] T. Yang, Z. Yang, X. Cheng, Y. Ding, Y. Fan, G. Liu, K. Zhang, S. Jin, X. Liu, Z. Qiao, Three-dimensional hierarchical urchin-like Nb_2O_5 microspheres wrapped with N-doped carbon: An advanced anode for lithium-ion batteries, J. Alloy. Compd. 876 (2021), 160145.

[49] N. Li, X. Lan, L. Wang, Y. Jiang, S. Guo, Y. Li, X. Hu, Precisely tunable T-Nb_2O_5 nanotubes via atomic layer deposition for fast-charging lithium-ion batteries, ACS Appl. Mater. Interfaces 13 (2021) 16445–16453.

[50] C. Niu, X. Liu, J. Meng, L. Xu, M. Yan, X. Wang, G. Zhang, Z. Liu, X. Xu, L. Mai, Three dimensional V_2O_5/NaV_6O_{15} hierarchical heterostructures: controlled synthesis and synergistic effect investigated by in situ X-ray diffraction, Nano Energy 27 (2016) 147–156.

[51] G. Nabi, M.A. Kamran, T. Alharbi, M. Rafique, M.B. Tahir, S. Hussain, N.R. Khalid, T. Iqbal, M. Shakil, C. Cao, A. YH_3, promoted palladium catalyst for reversible hydrogen storage of N-ethylcarbazole, Int. J. Hydrog. Energy 45 (2020) 33657–33662.

[52] Y. Zhang, P. Chen, Q. Wang, Q. Wang, K. Zhu, K. Ye, G. Wang, D. Cao, J. Yan, Q. Zhang, High-capacity and kinetically accelerated lithium storage in MoO_3 enabled by oxygen vacancies and heterostructure, Adv. Energy Mater. 11 (2021), 2101712.

[53] K. Wang, N. Li, L. Sun, J. Zhang, X. Liu, Free-standing N-doped carbon nanotube films with tunable defects as a high capacity anode for potassium-ion batteries, ACS Appl. Mater. Interfaces 12 (2020) 37506–37514.

[54] F. Xiong, Y. Jiang, L. Cheng, R. Yu, S. Tan, C. Tang, C. Zuo, Q. An, Y. Zhao, J. Gaumet, L. Mai, Bioinspired cellulose-integrated MXene-based hydrogels for multifunctional sensing and electromagnetic interference shielding, Interdiscip, Mater 1 (2022) 495–506.

[55] Y. Zheng, Z. Yao, Z. Shadike, M. Lei, J. Liu, C. Liu, Defect-concentration-mediated T-Nb_2O_5 anodes for durable and fast-charging Li-ion batteries, Adv. Funct. Mater. 32 (2022), 2107060.

[56] T.C. Canevari, L.T. Arenas, R. Landers, R. Custodio, Y. Gushikem, Simultaneous electroanalytical determination of hydroquinone and catechol in the presence of resorcinol at an SiO_2/C electrode spin-coated with a thin film of Nb_2O_5, Analyst 138 (2013) 315–324.

[57] W. van den Bergh, S. Wechsler, H.N. Lokupitiya, L. Jarocha, K. Kim, J. Chapman, K. E. Kweon, B.C. Wood, S. Heald, M. Stefik, Faster intercalation pseudocapacitance enabled by adjustable amorphous titania where tunable isomorphic architectures reveal accelerated lithium diffusivity, Batter. Supercaps 5 (2022), e202200056.

Jinghui Chen received her B.S. degree from Henan Polytechnic University in 2017 and M.S. degree from Wuhan University of Technology (WUT) in 2020. She is currently a Ph.D. candidate in Materials Science and Engineering at WUT. Her current research focuses on structure regulation of Niobium-based oxides and the mechanism of ultrafast and high-capacity lithium storage.

Jiashen Meng is now a postdoctoral research fellow at Peking University starting 2020 under the supervision of Prof. Quanquan Pang and Ruqiang Zou. He received his B.S. and Ph.D. degrees in materials science and engineering under the supervision of Prof. Liqiang Mai from Wuhan University of Technology in 2015 and 2020, respectively. In 2018–2019, He was a visiting Ph.D. student at MIT. His current research focuses on developing new nanomaterials and chemical solutions for extreme batteries.

Kang Han obtained her mater degree in Materials Science and Engineering from Wuhan University of Technology in 2019. His currently working toward the Ph.D. degree in Materials Science and Engineering at Wuhan University of Technology. His current research direction is the structure regulation and energy storage mechanism of key electrode materials for potassium-ion batteries based on small organic molecules.

Fang Liu obtained her mater degree in Materials Science and Engineering from Wuhan University of Technology in 2019. She is currently working toward the Ph.D. degree in Materials Science and Engineering at Wuhan University of Technology. Her current research focuses on in situ TEM and STEM based technique development and applications in energy storage materials.

Weixiao Wang received her M.S. degree from Xinyang Normal University in 2020. He is currently a Ph.D. candidate in Materials Science and Engineering at Wuhan University of Technology (WUT). Her current research focuses on the design and modification of molybdenum-based materials in multivalent ion batteries.

Qinyou An is Professor of Materials Science and Engineering at WUT. He received his Ph.D. degree from WUT in 2014. He carried out his postdoctoral research in the laboratory of Prof. Yan Yao at the University of Houston in 2014–2015. Currently, his research interest includes energy storage materials and devices.

Liqiang Mai is the Chair professor of Materials Science and Engineering at WUT, Dean of School of Materials Science and Engineering at WUT, Fellow of the Royal Society of Chemistry. He received his Ph.D. from WUT in 2004 and carried out his postdoctoral research at Georgia Institute of Technology in 2006–2007. He worked as an advanced research scholar at Harvard University and University of California, Berkeley. His current research interests focus on new nanomaterials for electrochemical energy storage and micro/nano energy devices.